nature communications

Article

https://doi.org/10.1038/s41467-024-50654-w

Ultrathin aerogel-structured micro/nanofiber metafabric via dual air-gelation synthesis for self-sustainable heating

Received: 3 February 2024

Accepted: 9 July 2024

Published online: 30 July 2024

Check for updates

Yucheng Tian[1], Yixiao Chen[1], Sai Wang[1], Xianfeng Wang[1], Jianyong Yu[1], Shichao Zhang[1] ✉ & Bin Ding[1,2] ✉

Incorporating passive heating structures into personal thermal management technologies could effectively mitigate the escalating energy crisis. However, current passive heating materials struggle to balance thickness and insulating capability, resulting in compromised comfort, space efficiency, and limited thermoregulatory performance. Here, a dual air-gelation strategy, is developed to directly synthesize ultrathin and self-sustainable heating metafabric with 3D dual-network structure during electrospinning. Controlling the interactions among polymer, solvent, and water enables the microphase separation of charged jets, while adjusting the distribution of carbon black nanoparticles within charged fluids to form fibrous networks composed of interlaced aerogel micro/nanofibers with heat storage capabilities. With a low thickness of 0.18 mm, the integrated metafabric exhibits exceptional thermal insulation performance (15.8 mW $m^{-1}K^{-1}$), superhydrophobicity, enhanced mechanical properties, and high breathability while maintaining self-sustainable radiative heating ability (long-lasting warming of 8.8 °C). This strategy provides rich possibilities to develop advanced fibrous materials for smart textiles and thermal management.

The escalating energy crisis, amplified by high energy consumption in heating, highlights the urgency of personal thermal management strategies to reduce the energy demand for indoor temperature regulation, by regulating the heat exchange between the human body and the environment[1,2]. Fibrous materials, with their unique accessibility and versatility, have gained prominence in the realm of thermal management materials, presenting innovative opportunities for enhancing energy efficiency and comfort in personal and industrial applications[3,4]. However, common fibrous materials exhibit uncontrolled pore structures, large pore size (commonly >50 μm), and limited porosity (typically <50%), which pose great challenges in achieving highly efficient thermal management performance[5,6]. In contrast to conventional fibers, micro/nanofibers with smaller diameters demonstrate significant potential in effective thermal management applications owing to their reduced pore size (always >2 μm) and enhanced porosity that effectively trap still air while significantly restricting heat transfer[7–9]. Recently, the 3D micro/nanofibrous sponges prepared by freeze-drying technology or electrospinning method, achieving a fluffy structure with improved porosity and uniform pore structure, which extends the heat transfer path and enhances thermal insulation (thermal conductivity of ~28 mW m^{-1} K^{-1})[10–13]. Nevertheless, the macropore network of these fibrous sponges is difficult to be refined, coupled with the inherent non-porous structure within the fibers, thereby limiting the effective suppression of air molecule heat transfer[14,15]. Furthermore, their excessive thickness (>20 mm) compromises sweat transmission and joint mobility of the body, leading to poor wet comfort (usually <2 kg m^{-2} d^{-1}) and space utilization, indicating the necessity for design enhancements that meet practical performance requirements[16,17].

[1]Innovation Center for Textile Science and Technology, College of Textiles, Donghua University, Shanghai, China. [2]School of Materials Science and Engineering, Shanghai University of Engineering Science, Shanghai, China. ✉e-mail: shichaozhang@dhu.edu.cn; binding@dhu.edu.cn

In comparison, aerogels, with their high porosity, and nanoscale pore size smaller than the mean free path of air molecules, have a thermal conductivity (~16 mW m^{-1} K^{-1}) that is even lower than that of static air (~24 mW m^{-1} K^{-1}), thus they are regarded as ideal material for thermal insulation[18–20]. Despite their efficient heat insulation properties, the inherent brittleness and hygroscopic nature of zero-dimensional aerogel powders impose limitations on their practicality in wearable technology[21–23]. To address the challenge, several aerogel materials composed of micro/nanofibers have been developed in recent years[18,24–26]. Typically, synthesized through freeze-spinning technique, aerogel fibers exhibit aerogel-like porous structure while maintaining the flexibility of traditional fibers[27–29]. Nevertheless, their suboptimal pore size (>500 nm) falls short in effectively impeding the movement of air molecules, a feat achieved by traditional silica aerogels with their significantly smaller pore size (<60 nm)[30–32]. Additionally, their large diameters (usually >200 μm) restrict the arrangement possibilities within fabric construction, leading to significant gaps, uncontrollable porous structure between fibers, and the resulting uneven thermal insulation[33,34]. These factors collectively contribute to moderate thermal conductivity and limited warmth retention, while the complex fabrication process further restricts their applications. Moreover, their inability to absorb solar and human body radiation leads to energy inefficiency, thereby limiting their broader application in thermal management as they can only impede heat transfer rather than store or regulate it[35,36]. Therefore, significant efforts are required to devise a simple and practical method, capable of preserving the fine-pore structure of aerogels and the flexibility of fibers, while ensuring effective utilization and storage of radiant energy.

After careful observation of sunflower growth, we discovered that heliotropism of the flower disc and the Fibonacci sequence of seeds allowed for optimal absorption and storage of light and chemical energy[37]. Inspired by these features, we in situ introduced seed-like and size-matching CB nanoparticles into the nanopores of transparent PMMA fibers by the humidity-induced heterogeneous electrospinning, resulting in the direct construction of the metafabric in one step. The unique Knudsen effect of interconnected nanopores (20–60 nm) and the multi-scattering of nanoparticles facilitate heat energy storage in aerogel fibers, achieving nanoscale Anderson localization within the multi-porous regions centered around nanoparticles. As a result, the obtained metafabric exhibits excellent passive heat storage performance with approximately ~65% radiant energy retention, while maintaining an ultra-low thermal conductivity of 15.8 mW m^{-1} K^{-1}. In addition, the physical interactions between nanoparticles and nanopores confer excellent mechanical properties upon the metafabric, enabling it to withstand 100 washing cycles and 1000 bucking cycles at a large strain of 50% without failure. Moreover, the metafabric also exhibits exceptional moisture permeability, as evidenced by its water vapor transmission (WVT) rate of 3.6 kg m^{-2} d^{-1}, along with superhydrophobic properties demonstrated by water contact angle (WCA) of 150°. Significantly, these characteristics are maintained while ensuring a low thickness (<0.2 mm). Consequently, this simple, scalable, and efficient metafabric for passive radiative heating not only significantly enhances clothing comfort in cold environments but also reduces energy consumption to help address the energy crisis.

Results

Design and processing of metafabric

We developed the aerogel-structured micro/nanofiber metafabric, similar to a sunflower, which could gather the energy from sun and human body while storing heat around the human body (Fig. 1a and Supplementary Fig. 1), achieving a wearable and long-lasting passive radiative heating. Our metafabric was designed based on three principles: (1) to maximize the collection of radiation, the metafabric must be able to absorb radiation in different wavelength bands simultaneously and efficiently; (2) to obtain heat storage in a limited space, the carrier of absorbers must be equipped with connected nanopores that locally suppress heat loss and reflect radiation from absorbers; (3) to be wearable comfortably and cope with different environments, the metafabric should be constructed using a fibrous network characterized by appropriate porous structure and hydrophobic external surface, while maintaining high porosity to facilitate efficient moisture transport. To satisfy the first requirement, as shown in Fig. 1a, CB nanoparticles (NPs) rich in π electronic structure and carbon-carbon bonds was selected as the absorber of solar and human body radiation[37]. Meanwhile, PMMA aerogel fibers composed of nanopores with size of 30–60 nm were set as the carrier of CB NPs (~60 nm), which can use the transparent properties of PMMA to increase the irradiation depth of radiation, and inhibit the movement of air molecules by Knudsen effect[30]. More importantly, the interconnective nanopores and uniformly embedded CB synergistically create an Anderson localization effect, as illustrated in Fig. 1a, effectively confining radiant heat within the fiber[38]. The last requirement was satisfied by designing well-connected micro/nanofiber network with properly sized pore, which reflects human body radiation through Mie scattering while ensuring the its softness, continuity, and mechanical enhancement[39].

The synthetic fabrication of metafabric involved four components: PMMA, CB, water-based fluoropolymer (WF), and DMAc, as presented in Supplementary Fig. 2. Initially, the hydrophobic agent is blended into the PMMA solution, which is then heated and stirred in water bath at 60 °C. To enhance the dispersion of CB, the mixture is subjected to ultrasonic treatment. Finally, the prepared solution was used to synthesize metafabric in one step by our unique dual air-gelation technique. This method allows PMMA molecular chains to arrange and entangle around solvent-enriched phases at the microscale, creating a porous structure within the fibers, while simultaneously forming a fibrous network through electrospinning at the macroscale. This network undergoes gelation upon entanglement, further forming the macroscopic aerogel-like porous structure between aerogel fibers. Manipulation of the phase inversion behavior of charged jets by electrospinning allowed for the direct creation of transparent and size-customized fibrous network composing of intertwined PMMA micro/nanofibers (Supplementary Fig. 3). With the addition of WF, moisture from the air permeates the hydrophobic jets, triggering phase separation. The PMMA molecular chains align and aggregate around the solvent-enriched phase, intertwining physically. This gelation process forms a molecular network within the jets, generating a nanoporous structure inside the fiber (Fig. 1a). Figure 1b–c shows the low thickness (~180 μm), scattering holes from fiber network, interconnective nanopores and evenly dispersed CB from aerogel fiber of the metafabric mentioned above. Further examination through transmission electron microscopy (TEM) uncovers the interconnected nature of these nanopores and the presence of CB nanoparticles embedded deeply in the aerogel fibers, as depicted in Fig. 1d. Complementing this, the optical and microscope photograph confirm the optical transparency of the PMMA fiber (Supplementary Fig. 4). The elemental composition and spatial distribution within the membranes were analyzed through energy-dispersive X-ray spectroscopy (EDS) mapping. This technique confirmed the uniform attachment of WF in the membranes, with the fluorine element being completely surrounded by carbon and oxygen, as illustrated in Fig. 1e. Raman spectroscopic analysis of the metafabric provides further insight into the metafabric (Supplementary Fig. 5). The smaller I_D (at 1350 cm^{-1}) to I_G (at 1583 cm^{-1}) peak ratio of 0.91, which is less than 1, indicates a higher degree of crystallinity and fewer structural defects in the material[40]. The innovative design of our metafabric with dual-aerogel networks provides an extended spectral response, covering a broad wavelength range from 0.1 to 15 μm (Fig. 1f). This enables the metafabric to absorb wavelengths from various sources, including the sun and the human body, across ultraviolet (UV), visible light (VL), near-

https://doi.org/10.1038/s41467-024-50654-w

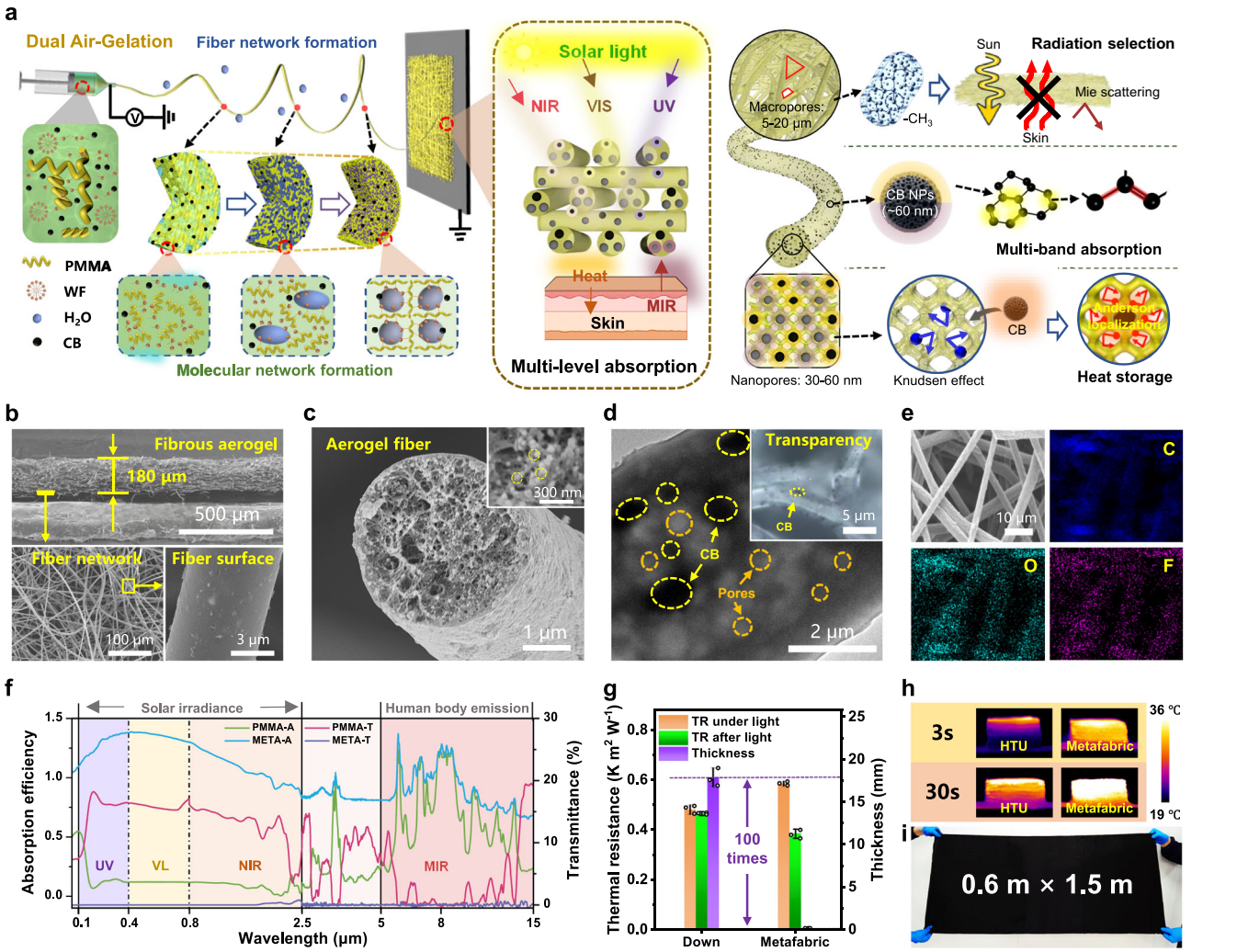

Fig. 1 | Proposed structure and properties of the metafabric. a Fabrication and structural features of the metafabric for self-sustainable radiative heating. **b**–**c** Microscopic architectures of the metafabric at various magnifications. **d** TEM image for PMMA/CB aerogel fibers. Inset: the optical paragraph of large-scale metaflim. **e** SEM-EDS images of the metafabric with corresponding elemental mapping images. **f** Calculated absorption (A) and transmittance (T) efficiencies for PMMA aerogel fibrous membranes (AFM) and metafabric. **g**–**h** Images demonstrating the thermal insulation performance and passive radiation heating capabilities of the metafabric. **i** Photograph of the large-sized metafabric. WF water-based fluoropolymer, CB carbon black, NIR near-infrared, VIS visible, UV ultra-violet, MIR mid-infrared, NPs nanoparticles, PMMA-A PMMA-absorption efficiency, TR thermal resistance, H-TU heating thermal underwear. Error bars in (g) represent the standard deviations of three replicates. Source data are provided as a Source Data file.

infrared ray (NIR), and mid-infrared ray (MIR) spectra. Owing to these tailored structures and physical properties, the metafabric exhibits thermal resistance (TR) comparable to down feathers, yet with a thickness only 1% of the latter, demonstrating the capacity for sustained heat generation, as shown in Fig. 1g. Moreover, the metafabric has a greater heating depth in the thickness direction and higher surface temperatures on both upper and lower layers compared to ordinary heating fabrics, as depicted in Fig. 1h. This indicates a more efficient absorption of light energy, showing the superior performance of our metafabric in heat management applications. In addition to its comprehensive performance, the metafabric can be produced on a large scale with dimensions of $0.6 \times 1.5\ m^2$ (Fig. 1i), based on our unique air-gelation technique.

Synthesis and nanostructures of metafabric

The synthesis of metafabric with the molecular networks and micro/nanofiber networks depended on water diffusion, molecular chain movement, and phase separation within the charged jets, as shown in Fig. 2a. Initially, in the absence of WF, which also acts as an anionic surfactant, results in the PMMA solution with higher surface tension. As water diffuses from the outside into the jet, the oxygen atoms in the ester groups ($COOCH_3$) of PMMA exhibit some hydrophilicity, attracting water to the PMMA surface. This interaction, coupled with solvent evaporation, results in the solidification of the jet into solid fibers. Upon the addition of a hydrophobic agent, the ionization of COO^- in the solution leads to a decrease in surface tension, enhancing the mobility of the molecular chains[41]. As water permeates, the fluorocarbon chains within the jet likely promote the aggregation of polymer molecules, leading to the formation of pores or microphase separation regions in the solution[42]. These pores are typically enveloped by polymer, while the hydrophobic agent is repelled to the edges, thereby uniformly distributing water and solvent in the spherical arrangement within the jet. This distribution facilitates phase separation, and the lower surface tension allows this process to occur more rapidly[43]. The stretching of the jet and the evaporation of the solvent culminate in the formation of a porous structure. The formation of an interconnected nanoscale porous structure composed of molecular chain networks is achieved following the disappearance of the solvent-rich phase and the solidification of the polymer-rich phase. This fabrication process is substantiated by SEM observations of the

https://doi.org/10.1038/s41467-024-50654-w

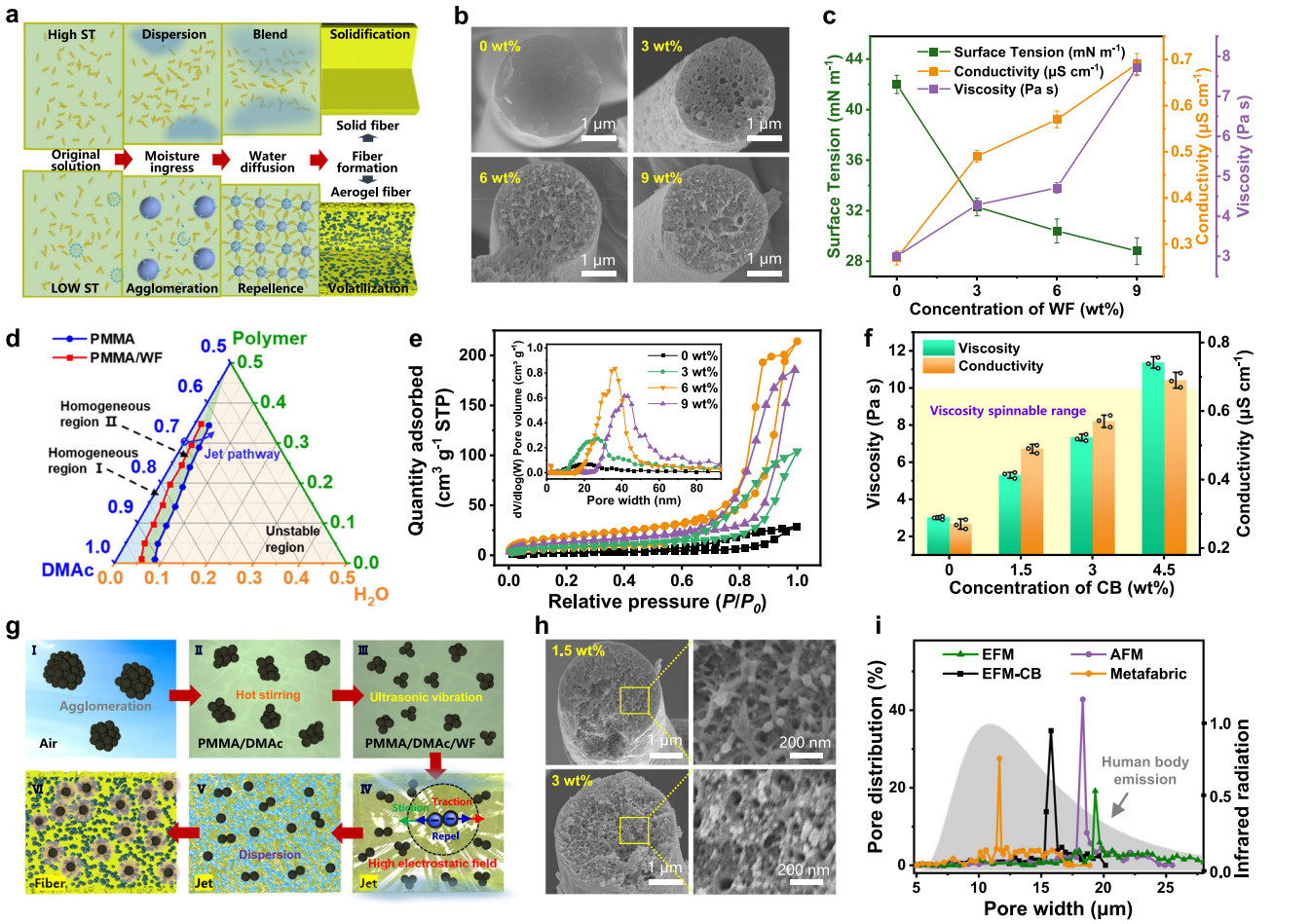

Fig. 2 | Manufacture and characterization of the metafabric. a Schematic illustrating the direct synthesis process of PMMA aerogel fiber **b** Representative FE-SEM images of the PMMA fiber at different WF contents. **c** Solution properties under different WF contents. **d** Cloud point curves for the PMMA/DMAc/H_2O system and PMMA/DMAc/WF/H_2O system, respectively, in the ternary phase diagram. **e** Nitrogen physisorption isotherms and DFT pore size distribution of the PMMA fibrous membranes with different concentrations of WF. **f** Solution properties under different CB contents. **g** Schematic diagram of the dispersion mechanism of CB in solution and spinning process. **h** Representative FE-SEM images of the PMMA aerogel fiber at different CB contents. **i** Positive Material Identification pore size distribution of prepared PMMA fibrous membranes with different structures. ST surface tension, WF water-based fluoropolymer, CB carbon black, EFM electrospun fibrous membranes, AFM aerogel fibrous membranes. Error bars in **c**, **f** represent the standard deviations of three replicates. Source data are provided as a Source Data file.

fiber cross-section, which show varying degrees of phase separation, as shown in Fig. 2b. With higher hydrophobic agent concentrations, the solution exhibits increased viscosity and electrical conductivity, alongside decreased surface tension. However, at the hydrophobic agent concentration of 9%, a sharp increase in both viscosity and conductivity is noted, which adversely affects the stability of the jet (Fig. 2c). Additionally, excessive surface tension can lead to overly rapid phase separation. This rapid separation prevents the timely formation of smaller pores, resulting in an increase in the diameter of the pores within the fibers, which is detrimental to the material inhibiting the movement of air molecules, ultimately leading to a decrease in thermal insulation performance[44].

The construction mechanism of our material can be further elucidated through an examination of the phase separation behavior exhibited by various PMMA solutions. As depicted in Fig. 2d, the introduction of the hydrophobic agent accelerates the precipitation of PMMA, expanding the non-stable region of solution phase separation and quickening the phase separation process. This is evidenced by the binodal curve of the hydrophobic solution, which shows the closer proximity to the initial composition compared to the hydrophilic solution, indicating a faster initiation rate of phase separation[45]. In order to further investigate the diverse pore structures of PMMA fibrous membranes, we conducted nitrogen physisorption analysis at a temperature of 77 K (Fig. 2e). The sorption behavior of PMMA aerogel micro/nanofiber membranes (AMMs) containing 6 wt% WF was characterized by a type II isotherm. Initial gradual N_2 uptake at $P/P_0 < 0.9$ indicated minimal interaction between nitrogen molecules and the fibers, reflecting a low micropore count in the AMMs. A marked N_2 absorption increase at higher relative pressures ($P/P_0 > 0.9$) highlighted the abundance of mesopores. Additionally, the distribution of water is more prevalent on the surface than in the interior of the jet, leading to the earlier solidification of the surface solution. This results in the formation of a porous structure in the inner layers, yielding fibers with a skin-core structure, consistent with the SEM observations, as shown in Fig. 2b. Supplementary Fig. 6 presents the quantification of the surface area and pore volume of AMMs, demonstrating a higher BET surface area of 68.38 $m^2 g^{-1}$ compared to the original PMMA fibrous membrane (9.35 $m^2 g^{-1}$). The pore size distribution (PSD) of the AMMs was determined using density functional theory (DFT) calculations. Interestingly, the PSD results align closely with the estimated size range observed in the SEM images (Fig. 2b). This alignment between theoretical calculations and empirical observations confirms the presence of abundant nanoscale pores, ranging from 30 to 60 nm, in the PMMA aerogel fibers.

https://doi.org/10.1038/s41467-024-50654-w

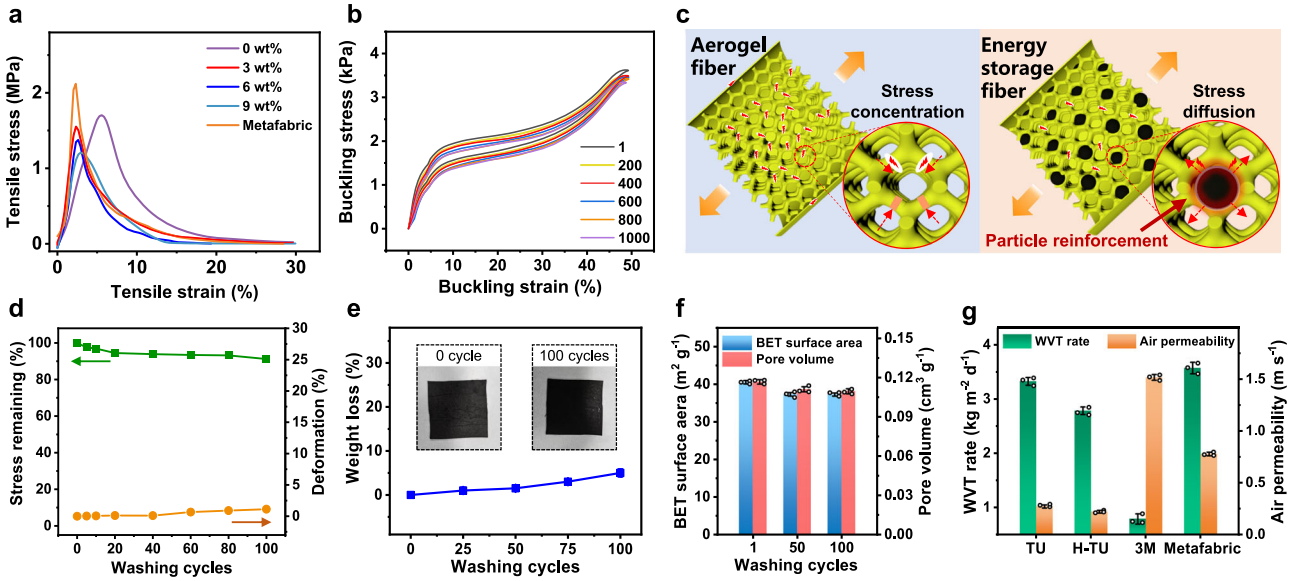

Fig. 3 | Mechanical properties and comfort performance of the metafabric. **a** Tensile stress-strain curves of PMMA fibrous membranes and metafabric. **b** Dynamic buckling fatigue tests for 1000 cycles at ε of 50%. **c** Schematic illustration of mechanical enhancement of aerogel fibers by nanoparticles. **d** Remaining compressive σ and plastic deformation of metafabric during 100 washing cycles. **e** Weight loss of the metafabric at 0, 25, 50, 75, and 100 washing cycles, respectively. **f** WVT rate and air permeability of different heating materials. **g** the waterproof and breathable capabilities of the metafabric. TU thermal underwear, H-TU heating thermal underwear. Error bars in (f, g) represent the standard deviations of three replicates. Source data are provided as a Source Data file.

Figure 2f illustrates the impact of varying CB concentrations on the viscosity and surface tension of the PMMA mixture. On the other hand, achieving a uniform distribution of CB is crucial for obtaining fibers with energy storage properties[46]. As shown in Fig. 2g, we propose the following hypotheses regarding the movement, force, and distribution of CB nanoparticles throughout the process of fiber formation in the solution. Initially, due to their high surface energy, CB nanoparticles tend to aggregate together. When introduced into the PMMA solution, the polar nature of DMAc (solvent) stabilizes the particles and prevents further aggregation. The addition of WF leads to a decrease in surface tension, while heating, stirring, and ultrasonic treatment result in an even dispersion of particles throughout the mixed solution. During the electrospinning process, water migrating from the outside to the inside of the jet prompts interactions between the hydrophobic nature of CB and the hydrophobic components[47]. The weakly negative charge on CB leads to mutual repulsion under an electric field, further dispersing the particles. As the particle size of CB is close to that of the pores, when the jet undergoes phase separation to form aerogel fibers, CB becomes embedded in some of the nanopores, forming nanoscale local closed-pore structures in tandem with the nanopores. Moreover, the PMMA aerogel fibers have fewer nanoparticles at lower concentrations of CB, preventing closed-pore structures and radiation absorption (Fig. 2h). However, at 3 wt% CB, nanopores are embedded with CB particles, forming effective nanoscale structures without particle aggregation. Increasing CB to 4.5 wt% leads to a viscosity exceeding 1.1 Pa s, surpassing the spinnable range for electrospinning solutions, preventing continuous fiber formation. As presented in Fig. 2i, the metafabric exhibits a fiber inter-pore distribution that closely matches the wavelengths of human body radiation, enabling it to absorb body radiation while reflecting part of the mid-infrared emissions through Mie scattering[39].

Mechanical performances of metafabric

Conventional supercritical drying methods yield silica aerogels and fibrous sponges obtained by freeze-drying that lack stretchability, failing to meet the mechanical requirements for human consumption, which is a crucial challenge that must be overcome in the development of aerogel fibers[48]. The tensile stress–strain curves of PMMA electrospun fibrous membranes (EFM) and metafabric (Fig. 3a) demonstrate a notable negative correlation between tensile strength and WF content, but a positive correlation with the addition of CB. First, the hydrophobic agent causes the formation of porous structure inside PMMA fibers, resulting in a slight decrease in their tensile properties. Surprisingly, adding an optimal amount of CB (3 wt%) enhances the tensile fracture stress by approximately 54%, increasing it from 1.37 to 2.12 MPa, even surpassing the strength of solid PMMA fibers. Then, the metafabric displayed no visible plastic deformation and effectively maintained its initial maximum stress when subjected to 1000 bending deformation cycles at buckling strain of 50%, indicating excellent fatigue resistance against repetitive bending and buckling, as depicted in Fig. 3b. Based on these findings, we propose a particle mechanics enhancement mechanism (Fig. 3c). In conventional aerogel fibers under tensile stress, the stress initially concentrates on the polymer pore walls, leading to their fracture followed by the breakdown of the surface layer, culminating in total fiber failure. In contrast, for energy storage fibers, tensile stress initially transfers from the pore walls to the CB nanoparticles embedded within the pores. This dispersion of stress makes the pore walls more resistant to fracture, ultimately enhancing the overall mechanical properties of the fibers[46]. The durability of the metafabric was rigorously tested through the 100-cycle washing process with a compressive strain (ε) of 50%, as presented in Fig. 3d. The plastic deformation after these cycles was only 6.2%, which only exhibited a slight increase than the values without washing. Furthermore, the metafabric demonstrated stability, maintaining static stress levels between 100% to 91% and exhibiting nearly no plastic deformation (<1%) throughout the cyclic washing process. Additionally, after 100 washing cycles, the metafabric showed almost no change in either size or weight (weight loss <5%), indicating a robust integration of CB nanoparticles within the PMMA aerogel fibers, as shown in Fig. 3e. This stability is attributed to the hydrophobic interactions between CB, PMMA, and WF, resulting in a strong bond within the fiber structure[46]. The BET surface area and pore volume of the metafabric also exhibited minimal changes post-washing, underscoring its exceptional reusability (Fig. 3f).

Moreover, the metafabric exhibits the WVT rate of ~3.6 kg m^{-2} d^{-1}, which is 4.5 times higher than that of 3 M Thinsulate insulation

https://doi.org/10.1038/s41467-024-50654-w

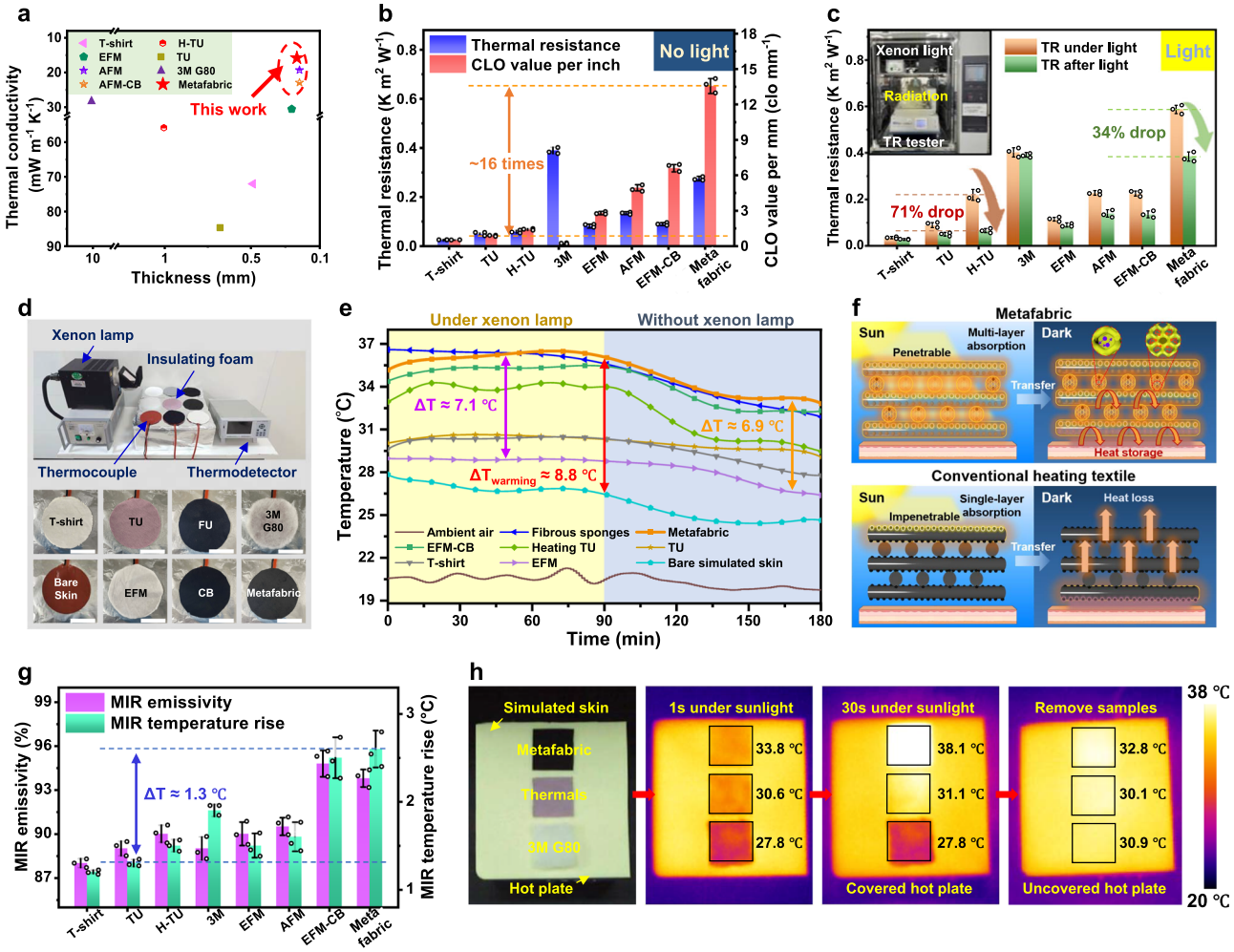

Fig. 4 | Thermal analysis to determine the metafabric heating performance. **a**–**b** Comparison of thermal insulation performance and thickness for the different thermal management materials and the metafabric under no light conditions. **c** Thermal resistance under different lighting conditions. **d** Photo of the thermal measurement system used to characterize the radiative heating performance. Scale bars, 5 cm. **e** Temperature difference of skin simulators under different fabric samples in same location. **f** Comparison of solar energy absorption between the metafabric and traditional heating textile. **g** FIR emissivity and temperature rise of different heating materials. **h** Optical and infrared images of the hot plate before and after covering different materials. CB carbon black, EFM electrospun fibrous membranes, AFM aerogel fibrous membranes, TU thermal underwear, H-TU heating thermal underwear, TR thermal resistance, MIR mid-infrared. Error bars in (b, c, g) represent the standard deviations of three replicates. Source data are provided as a Source Data file.

materials and surpasses other thermal insulation textiles. Moreover, the metafabric exhibits good flexibility (Supplementary Fig. 7), and its breathability significantly exceeds that of other commercial fabrics, making it a superior choice in terms of air permeability (Fig. 3g). This suggests that the metafabric not only excels in thermal insulation but also meets the everyday comfort requirements of consumers. Compared to the traditional textile materials, as illustrated in Supplementary Fig. 3, using PMMA as a carrier for heating particles significantly enhances radiation transmittance. Specifically, within the 200–800 nm wavelength range, the average visible light emissivity of the metafabric reaches an impressive 0.9. This represents an increase of approximately five times and four times compared to EFM (0.18) and TH (0.24), respectively (Supplementary Fig. 8–9). Moreover, in comparison to commercially available high-end radiative heating fabrics, it has achieved a 50-fold reduction in thickness while enhancing its radiation absorption efficiency by 30%. These findings highlight the exceptional capability of metafabric to absorb solar radiation, demonstrating its superior performance in radiative heating. As shown in Supplementary Fig. 10–11, under the synergistic hydrophobic effects of CB (carbon-carbon bonds) and WF (carbon-fluorine chains), this material exhibits an extraordinary superhydrophobic property, characterized by an impressive contact angle of 150°, significantly enhancing durability and providing exceptional water and stain resistance[49]. The metafabric, in conjunction with its exceptional moisture permeability, offers comprehensive functional and comfortable protection for human activities (Supplementary Fig. 12).

Thermal regulation performance of metafabric

In view of the dual-aerogel network structure, exceptional radiation absorbency, and superior comfort, the metafabric exhibits promising potential for applications in smart textiles and personal thermal management. First, we studied the thermal management performance of the metafabric in a light-free environment. As illustrated in Fig. 4a and Supplementary Fig. 13, the metafabric, with a mere thickness of 180 μm and high porosity (91.3%), exhibits an ultra-low thermal conductivity (15.8 mW m^{-1} K^{-1}), significantly lower than other insulation materials and even below that of stationary air. The thermal conductivity of a material alone is insufficient to fully evaluate its heat transfer capabilities, as this measure could not show the effects of radiation and thermal convection on thermal management[18]. Therefore, we set up a thermal resistance tester and xenon lamp experimental apparatus in a controlled temperature and humidity indoor

environment to evaluate the comprehensive insulation capability of materials under different lighting conditions (Fig. 4b–c). The thermal resistance of AFM increased by 73% in the absence of sunlight due to its nanoporous structure. The metafabric exhibited a thermal resistance more than twice that of AFM, attributed to the absorption of mid-infrared radiation by CB and its synergistic effect with nanopores (Fig. 4b). Moreover, the metafabric's thermal resistance is an impressive 16 times greater than that of commercial thermal underwear, while its thickness is only one-third of the latter. This suggests that the nanopores inside the aerogel fibers efficiently prevents air molecules from moving and from transferring heat by the Knudsen effect (Supplementary Fig. 14). As demonstrated in Fig. 4c and Supplementary Fig. 15, the metafabric dramatically increased to 0.588 K m^2 W^{-1} under simulated sunlight, owing to the absorption of visible and near-infrared light by the carbon black. At this stage, the thermal resistance of the metafabric was 178 times greater than a standard T-shirt and about 46% higher than a 3 M fibrous sponge, while being only one percent as thick, highlighting its exceptional ultra-thin insulation and heating capabilities. Upon turning off the simulated sunlight, the thermal resistance of the metafabric decreased to 65% of its maximum value but remained 40% higher compared to the scenario with continuous absence of sunlight. This performance contrasts with that of ordinary heating fabrics, which showed a decrease to 29% of their original thermal resistance, nearly the same as their performance without sunlight exposure at the beginning.

Furthermore, we conducted direct thermal measurements under a Xenon lamp to evaluate the outdoor radiative heating performance of our metafabric. The temperature of each fabric sample was accurately monitored affixing three K-type thermocouples onto a copper plate, ensuring uniformity in thermal measurements (Fig. 4d). Within 90 minutes of activation by simulated sunlight, the temperature of the metafabric was consistently higher compared to other materials. As shown in Fig. 4e, it was approximately 2.3, 5.6, 5.8, 7.2, and 9.3 °C higher than that of the Heating TU (commercially thermal underwear with passive heating functionality), TU, T-shirt, EFM, and bare skin simulators, respectively. During this phase, both the metafabric and the 3 M fibrous sponges, which are 100 times thicker, maintained the highest temperatures. On the other hand, the 3 M fibrous sponges maintained the simulated skin surface temperature primarily due to their high thickness, which provides a prolonged heat transfer path[50]. During the 90 min following the cessation of simulated sunlight, the temperature of the metafabric remained significantly higher compared to other materials. Specifically, it was about 3.8, 4.2, 4.9, 6.2, and 9.0 °C higher than the Heating TU, TU, T-shirt, EFM, and bare skin simulators, respectively (Fig. 4e). Moreover, over the entire 3-h period of the simulated sunlight exposure and shutdown, the temperature of the metafabric decreased by only 2.2 °C. In comparison to conventional radiative heating materials like HTU, which is six times thicker and experienced a temperature drop of 3.7 °C, the metafabric showed a more than 71% improvement in light energy storage efficiency, validating the energy storage characteristics of its unique structure. The translucency of PMMA, combined with the Anderson positioning induced by the small-sized nanopores and carbon black nanoparticles, facilitates radiation penetration into the fiber network and enables efficient absorption and storage of thermal radiation by the metafabric, as depicted in Fig. 4f.

Besides, we investigated the absorptive capability of metafabric for human-emitted radiation within the 5 to 14 μm wavelength spectrum (Fig. 4g). The test results showed that the metafabric had a higher infrared emissivity compared to ordinary heating fabrics. The rate of infrared temperature rise was over 73% higher than that of ordinary heating fabrics, demonstrating the superior mid-infrared absorption capability of the metafabric. To vividly demonstrate the heating performance of the metafabric, we utilized a heating plate and silicone pad to simulate human skin and employed an infrared thermal imaging camera to observe the surface temperature under different lighting conditions, as depicted in Fig. 4h. The thermal camera revealed a substantial temperature difference between the metafabric (38.1 °C) and TU (31.1 °C) after 30 s of illumination. After removing the materials, the simulated skin covered by the metafabric was 2.7 °C warmer than that covered by TU and nearly 2 °C warmer than that covered by the 3 M fibrous sponge, suggesting that the metafabric could be an effective alternative to thicker insulating materials. As illustrated in Supplementary Fig. 14, compared to conventional fabrics, porous fibers, and aerogel fibers, our energy storage fiber possesses both the ability to suppress heat at the molecular level and slow-release heating functionality, offering a distinct advantage in thermal management applications[51]. We also compared our metafabric with commercial heating textiles in terms of adiabaticity, scalability, flexibility, penetrability, radiation absorption, lightness, thinness, and scalability[52]. In comparison (Fig. 4i), our metafabric exhibits exceptional hydrophobicity, more efficient radiation absorption, and better warmth retention performance than commercial thermal insulation materials at a low thickness.

Discussion

We have presented the facile methodology for the direct synthesis of self-sustainable radiative heating metafabric based on aerogel-structured micro/nanofibers using the unique dual air-gelation technique, which overcomes the longstanding challenge in practical application of fragile aerogel in thermal managament textiles. By regulating water diffusion, molecular chain movement, and phase separation within the charged jets, the dual-aerogel-structured metafabric was assembled. This metafabric was fabricated through the entanglement and interlacing of PMMA/CB aerogel micro/nanofibers, aiming to achieve a synergistic effect in terms of radiation absorption, insulation, and heating properties. With a thin overall thickness of only 180 μm, our energy storage aerogel micro/nanofibers exhibit far lower thermal conductivity (15.8 mW m^{-1} K^{-1}) and a higher heating effect (8.8 °C) compared with the existing aerogel fibrous materials. Benefiting from the Anderson localization formed by nanopores (30–60 nm) and CB, the metafabric demonstrates self-sustainable radiative heating (>65% solar heat retention rate). Together with its other outstanding features such as enhanced mechanical properties (plastic deformation of nearly 0% over 1000-cycle washing), super hydrophobicity (WCA of 150°), high moisture permeability (WVT of 3.6 kg m^{-2} d^{-1}), and strong self-adaptability, with more optimization, we believe that the metafabric could demonstrate potential applications in various emerging applications such as smart textiles and personal thermal management.

Methods

Materials

PMMA powder (M_w = 500000) was supplied by Shanghai yuanye Bio-Technology Co., Ltd. Fluorinated polyurethane (FPU, QF66) was obtained from Shanghai Taifu Chemical Co., Ltd. DMAc were provided by Shanghai Aladdin Chemistry Co., Ltd. Carbon black NPs (CB, d ~ 60 nm), were bought from Tianjin Zhengningxin Material Technology Co., Ltd.

Fabrication of the metafabric

PMMA powder was dissolved in DMAc to form a 30 wt% solution, followed by the addition of hydrophobic agents at 0, 1.5, 3, and 4.5 wt% concentrations. Then, CB particles were added at 0, 3, 6, and 9 wt% concentrations. After stirring at room temperature for 8 h, the mixture underwent an hour of ultrasonic treatment. Afterwards, the aerogel fiber membranes were prepared using an electrospinning platform equipped with a humidity-controlled system, applying 30 kV voltage and extruding the solutions at 4 mL h^{-1}. Electrospinning was conducted in a lab at a constant 23 ± 2 °C and 55 ± 5% relative humidity.

Characterization

Microstructure analyzed using FE-SEM (Hitachi S-4800, Japan), TEM (FEI Tecnai F20, USA), and EDS (Bruker 610 M, USA). Raman spectroscopy was performed using a LabRAM HR Evolution system at 532 nm excitation. Pore structure evaluated using a capillary flow porometer (CFP-1100AI, USA) and physisorption analyzer (Micromeritics ASAP 2460, USA). Porosity was determined through the equation: porosity = $(\rho_0\text{-}\rho)/\rho_0\times100\%$, where ρ represents the bulk density of the fibrous structures and ρ_0 the density of polymer chips. Viscosity, conductivity, surface tension measured using a rotary viscometer (LVDV-1T), conductivity meter (FE30), and tensiometer (QBZY). Mechanical properties were assessed with a dynamic mechanical analyzer (Q850, TA Instruments, USA). Water vapor permeability tested using moisture permeability tester (YG601H, China), upright cup configuration. The WCA was measured with a goniometer (Kino SL200B, USA). UV-vis-NIR absorbance of the metafabric was recorded using a spectrophotometer (UV-3600, Shimadzu Ltd., Japan) with an integrating sphere. Solar illumination tests were conducted using a solar simulator (PLS-SXE 300, Perfectlight Ltd., China) with adjustable light intensity (300–600 W m^{-2}) and the lamp positioned 55–95 cm away from the sample. Infrared images captured with an IR camera (Fluke-TiS75, USA). FTIR analyses were conducted on a Nicolet iS50 Spectrometer (Thermo Fisher Scientific Inc., USA), equipped with a Pike golden hemisphere integrating sphere, an MCT (Mercury Cadmium Telluride) detector cooled with liquid nitrogen, and a gold reference for background. The far-infrared emissivity and temperature increase measured using emissivity tester (DR915G, Wenzhou Darong Textile Instrument Co. Ltd., China) and temperature-rise tester (DR915W, Wenzhou Darong Textile Instrument Co. Ltd., China). The thermal constants analyzer (Hot Disk TPS2500, Sweden) was utilized to evaluate the thermal conductivity. The humidity and temperature was kept at 50 ± 5% and 23 ± 2 °C, respectively; the air of the testing condition was kept relatively still by using windshield. The thermal resistance of samples was carried out by the textile thermal transmittance tester (YG606E-II, China). The humidity, temperature, and airspeed of the testing condition were set at 65 ± 2%, 20 °C, and 1 m s^{-1}, respectively, according to GB/T 11048-2018.

Data availability

All data generated in this study are provided in the Source Data file. Source data are provided with this paper.

References

1. Jessoe, K. & Moore, F. C. The energy costs of climate change. *Nature* **598**, 262–263 (2021).
2. Tang, K. et al. Temperature-adaptive radiative coating for all-season household thermal regulation. *Science* **374**, 1504–1509 (2021).
3. Wang, Z. et al. Self-sustaining personal all-day thermoregulatory clothing using only sunlight. *Science* **382**, 1291–1296 (2023).
4. Gong, X. et al. High-performance liquid-Repellent and thermal-wet comfortable membranes using triboelectric nanostructured nanofiber/meshes. *Adv. Mater.* **35**, 2305606 (2023).
5. Hsu, P.-C. et al. A dual-mode textile for human body radiative heating and cooling. *Sci. Adv.* **3**, e1700895 (2017).
6. Chan, K.-Y. et al. Scalable anisotropic cooling aerogels by additive freeze-casting. *Nat. Commun.* **13**, 5553 (2022).
7. Cheng, X., Liu, Y.-T., Si, Y., Yu, J. & Ding, B. Direct synthesis of highly stretchable ceramic nanofibrous sponges via 3D reaction electrospinning. *Nat. Commun.* **13**, 2637 (2022).
8. Ruckdeschel, P., Philipp, A. & Retsch, M. Understanding thermal insulation in porous, particulate materials. *Adv. Funct. Mater.* **27**, 1702256 (2017).
9. Hui, Liu et al. Electrospun nanofiber as building blocks for high-performance air filter: a review. *Nano Today* **55**, 102161 (2024).
10. Zong, D. et al. Direct synthesis of elastic and stretchable hierarchical structured fiber and gaphene-based sponges for noise reduction. *ACS Nano* **17**, 17576 (2023).
11. Wu, H., Cai, H., Zhang, S., Yu, J. & Ding, B. Ultralight, superelastic, and washable nanofibrous sponges with rigid-flexible coupling architecture enable reusable warmth retention. *Nano Lett.* **22**, 830–837 (2022).
12. Chang, X. et al. Multiscale interpenetrated/interconnected network design confers all-carbon aerogels with unprecedented thermo-mechanical properties for thermal insulation under extreme environments. *Adv. Mater.* **36**, 2308519 (2023).
13. Zong, D. et al. Flexible ceramic nanofibrous sponges with hierarchically entangled graphene networks enable noise absorption. *Nat. Commun.* **12**, 6599 (2021).
14. Wang, S. et al. Direct synthesis of polyimide curly nanofibrous sponges for high-performance thermal insulation under extreme temperature. *Adv. Mater.* **36**, 2313444 (2023).
15. Si Y., Wang X., Dou L., Yu J., Ding B. Ultralight and fire-resistant ceramic nanofibrous sponges with temperature-invariant superelasticity. *Sci. Adv.* **4**, eaas8925 (2018).
16. Wicklein, B. et al. Thermally insulating and fire-retardant lightweight anisotropic foams based on nanocellulose and graphene oxide. *Nat. Nanotechnol.* **10**, 277–283 (2015).
17. Zhao, S., Malfait, W. J., Guerrero-Alburquerque, N., Koebel, M. M. & Nyström, G. Biopolymer aerogels and foams: Chemistry, properties, and applications. *Angew. Chem. Int. Ed.* **57**, 7580–7608 (2018).
18. Zhu, Y. et al. A breathable, passive-cooling, non-inflammatory, and biodegradable aerogel electronic skin for wearable physical-electrophysiological-chemical analysis. *Adv. Mater.* **35**, 2209300 (2023).
19. Qin, B. et al. A petrochemical-free route to superelastic hierarchical cellulose aerogel. *Angew. Chem., Int. Ed.* **62**, e202214809 (2023).
20. Wang, S. et al. Ultralight and superelastic curly micro/nanofibrous aerogels by direct electrospinning enable high-performance warmth retention. *Small* **19**, 2302835 (2023).
21. Hu, Z. et al. Natural silk nanofibril aerogels with distinctive filtration capacity and heat-retention performance. *ACS Nano* **15**, 8171–8183 (2021).
22. Zhang, F., Yu, J., Si, Y. & Ding, B. Meta-aerogel ion motor for nanofluid osmotic energy harvesting. *Adv. Mater.* **35**, 2302511 (2023).
23. Zhou, J. & Hsieh, Y.-L. Nanocellulose aerogel-based porous coaxial fibers for thermal insulation. *Nano Energy* **68**, 104305 (2020).
24. Zong, D. et al. Gradient pore structured elastic ceramic nanofiber aerogels with cellulose nanonets for noise absorption. *Adv. Funct. Mater.* **33**, 2301870 (2023).
25. Pirzada, T., Ashrafi, Z., Xie, W. & Khan, S. A. Cellulose silica hybrid nanofiber aerogels: from sol–gel electrospun nanofibers to multifunctional aerogels. *Adv. Funct. Mater.* **30**, 1907359 (2019).
26. Li, L. et al. Large-scale assembly of isotropic nanofiber aerogels based on columnar-equiaxed crystal transition. *Nat. Commun.* **14**, 5410 (2023).
27. Cui, Y., Gong, H., Wang, Y., Li, D. & Bai, H. A thermally insulating textile inspired by polar bear hair. *Adv. Mater.* **30**, e1706807 (2018).
28. Liu, Z., Lyu, J., Fang, D. & Zhang, X. Nanofibrous kevlar aerogel fibers for thermal insulation in harsh environments. *ACS Nano* **13**, 5703–5711 (2019).
29. Li, G., Hong, G., Dong, D., Song, W. & Zhang, X. Multiresponsive graphene-aerogel-directed phase-change smart fibers. *Adv. Mater.* **30**, 1801754 (2018).
30. Kara, V., Yakhot, V. & Ekinci, K. L. Generalized Knudsen number for unsteady fluid flow. *Phys. Rev. Lett.* **118**, 074505 (2017).
31. Wu, M. et al. Biomimetic, knittable aerogel fiber for thermal insulation textile. *Science* **382**, 1379–1383 (2023).
32. Sheng, Z. et al. The rising aerogel fibers: status, challenges, and opportunities. *Adv. Sci.* **10**, 2205762 (2023).

33. Hou, Y., Sheng, Z., Fu, C., Kong, J. & Zhang, X. Hygroscopic holey graphene aerogel fibers enable highly efficient moisture capture, heat allocation and microwave absorption. *Nat. Commun.* **13**, 1277 (2022).
34. Li, X., Dong, G., Liu, Z. & Zhang, X. Polyimide aerogel fibers with superior flame resistance, strength, hydrophobicity, and flexibility made via a universal sol-gel confined transition strategy. *ACS Nano* **15**, 4759 (2021).
35. Tian, Y. et al. Ultrathin aerogel micro/nanofiber membranes with hierarchical cellular architecture for high-performance warmth retention. *ACS Nano* **17**, 25439–25448 (2023).
36. Peng, Y. & Cui, Y. Advanced textiles for personal thermal management and energy. *Joule* **4**, 724–742 (2020).
37. Qin, J. et al. The bionic sunflower: a bio-inspired autonomous light tracking photocatalytic system. *Energy Environ. Sci.* **14**, 3931–3937 (2021).
38. Chakrabarty, R. K. et al. Shortwave absorption by wildfire smoke dominated by dark brown carbon. *Nat. Geosci.* **16**, 683–688 (2023).
39. Yamilov, A. et al. Anderson localization of electromagnetic waves in three dimensions. *Nat. Phys.* **19**, 1308–1313 (2023).
40. Cihan, A. F., Curto, A. G., Raza, S., Kik, P. G. & Brongersma, M. L. Silicon Mie resonators for highly directional light emission from monolayer MoS_2. *Nat. Photonics* **12**, 284–290 (2018).
41. Zhang, M. et al. Remediation of heavily PAHs-contaminated soil with high mineral content from a coking plant using surfactant-enhanced soil washing. *Sci. Total Environ.* **909**, 168499 (2024).
42. Li, H. et al. A novel modification to boron-doped diamond electrode for enhanced, selective detection of dopamine in human serum. *Carbon* **171**, 16–28 (2021).
43. Seong, H.-G., Fink, Z., Chen, Z., Emrick, T. & Russell, T. P. Bottlebrush polymers at liquid interfaces: Assembly dynamics, mechanical properties, and all-liquid printed constructs. *ACS Nano* **17**, 14731–14741 (2023).
44. Apostolopoulou-Kalkavoura, V., Munier, P. & Bergstrom, L. Thermally insulating nanocellulose-based materials. *Adv. Mater.* **33**, e2001839 (2021).
45. Poudyal, M. et al. Intermolecular interactions underlie protein/peptide phase separation irrespective of sequence and structure at crowded milieu. *Nat. Commun.* **14**, 6199 (2023).
46. Windey, R., AhmadvashAghbash, S., Soete, J., Swolfs, Y. & Wevers, M. Ultrasonication optimisation and microstructural characterisation for 3D nanoparticle dispersion in thermoplastic and thermosetting polymers. *Compos. Pt. B-Eng.* **264**, 110920 (2023).
47. Lu, H. et al. Phase-separation mechanism for c-terminal hyperphosphorylation of RNA polymerase II. *Nature* **558**, 318–323 (2018).
48. Yang, S., Xie, C., Qiu, T. & Tuo, X. The aramid-coating-on-aramid strategy toward strong, tough, and foldable polymer aerogel films. *ACS Nano* **16**, 14334–14343 (2022).
49. Zhao, S. et al. Golden section criterion to achieve droplet trampoline effect on metal-based superhydrophobic surface. *Nat. Commun.* **14**, 6572 (2023).
50. Saleta Reig, D. et al. Unraveling heat transport and dissipation in suspended $MoSe_2$ from bulk to monolayer. *Adv. Mater.* **34**, 2108352 (2022).
51. Cai, L. et al. Warming up human body by nanoporous metallized polyethylene textile. *Nat. Commun.* **8**, 496 (2017).
52. Wang, Z. Q. et al. Enhancing the radiative heating performance of down fibers by layer-by-layer self-assembly. *J. Clean. Prod.* **298**, 126760 (2021).

Acknowledgements

This work was supported by the National Key Research and Development Program of China (Nos. 2022YFB3804903 and 2022YFB3804900), the National Natural Science Foundation of China (Nos. 51925302 and 52273053), the Shanghai Committee of Science and Technology (No. 21ZR1402600), and the Fundamental Research Funds for the Central Universities (2232023Y-01).

Author contributions

B.D., S.Z., and Y.T. designed the research and wrote the manuscript. Y.T. and J.Y. involved the analysis of performance data. C.Z., Y.T., and S.W. prepared the samples and performed structural analysis. Y.T., X.W., and Y.C. tested the warmth retention performance and other properties.

Competing interests

The authors declare no competing interests.

Additional information

Supplementary information The online version contains supplementary material available at https://doi.org/10.1038/s41467-024-50654-w.

Correspondence and requests for materials should be addressed to Shichao Zhang or Bin Ding.

Peer review information *Nature Communications* thanks the anonymous reviewer(s) for their contribution to the peer review of this work. A peer review file is available.